NUMERICAL SIMULATION AND VALIDATION OF QUASI STEADY STATE METHOD FOR DUAL SIZES CALCINATION IN A PARALLEL FLOW REGENERATIVE LIME KILN

Shaopei DUAN [*], Zhengzhe FANG, Baokuan LI

[*]*School of Metallurgy,Northeastern University,Shenyang 110819,China*

[*] Corresponding author; E-mail:duanshaopei_neu@163.com

As an essential slagging raw material in blast furnace ironmaking, quicklime, which requires high chemical activity, is produced in parallel flow regenerative (PFR) lime kilns. The PFR lime kiln supports a wide range of fuels and can calcine a wide range of particle sizes while maintaining a high reactivity, which enhances the high temperature hard-burnt issue caused by rotary kilns.In this study, the bed porosity under dual sizes structure has been obtained with the help of Discrete Element Model (DEM) based on Porous Medium Model (PMM), and the distribution of gas-solid temperature and decomposition rate in dual sizes PFR lime kiln under the condition of low grade fuel has been simulated by numerical method, and the accuracy of the model has been verified by the monitoring data of control system. The results showed that calcination with 100+30 mm dual sizes improved the production efficiency compared to single sizes.

Keywords*: PFR lime kiln, quasi steady state, dual sizes, lime calcination, numerical simulation*

1. Introduction

As an important material in blast furnace ironmaking, soft burnt lime has an irreplaceable role. Due to the soft burnt lime grain size, lattice instability, high porosity, large reaction area and other characteristics, can quickly penetrate into the lime void with FeO, MnO, CaF_2, etc. to form a lower melting point of the melt and melt into slag. Under the same operating conditions, adding soft burnt lime 2~3 min after slagging, which shortens the melting time [1,5,6]. Soft burnt lime has a low hard burnt rate, and lime absorbs less heat, which can have a reduction in heat loss and increase the heat rate. If soft burnt lime is used, the lime dosage is reduced, so that the generation of steel slag is also correspondingly reduced by 12~18 kg/t. The amount of slag is reduced, the amount of slag spraying is also reduced accordingly, and the reduction of slag reduces the iron loss, and its comprehensive result is that the molten steel yield is increased by 0.5%~1% [2,4]. Due to the soft burnt lime itself contains few impurities, low sulfur and phosphorus content, stable composition, so it is easy to steelmaking operation, and help to improve and improve the quality of steel. Add soft burnt lime, fast melting into the slag CaO can quickly neutralize the acidity of the slag, and at the same time shorten the smelting time, accordingly improve the age of the furnace, and is conducive to the protection of the furnace lining, generally improve the age of the furnace by

20% [3]. In summary, the use of soft burnt lime can shorten the blowing time; desulfurization, dephosphorization fruit increase; smelting high quality steel proportion increase. Thus, it can reduce the lime consumption, scrap consumption, fluorite consumption and other related materials, saving costs and economic investment.

Two-dimensional mathematical models of the limestone calcination process began to appear in the 1990s [7] and were applied to the production and optimization of rotary kilns, which were widely dominant calcination equipment at that time [8,9,10]. With the continuous development of Computational Fluid Dynamics (CFD), commercial software has contributed to the development of mathematical models, which have evolved to a three-dimensional stage [11] and are increasingly used in more flexible and energy-efficient lime kilns [12,13,14].

PFR lime kiln has gained greater acceptance in the steel industry for its advantages such as energy saving and high product activity after solving its bottleneck of lower capacity [15]. Due HaiDo et al. conducted a simulation study for the energy conversion and calcination process of PFR lime kiln by using a porous medium model [16,17], and considered the role of particle size on the decomposition research of lime, which inspired for the further exploration of the design and energy utilization of PFR lime kilns [18,19,20]. Since then, studies on the calcination process of PFR lime kilns based on porous media modeling have gradually increased [21,22]. Owing to the wide range of fuels supported by PFR lime kilns, studies on the calcination effect of low calorific value fuels have also appeared [23,24,25].

In addition to fuel type, particle size is also an important parameter that affects the calcination effect. With the realization of the discrete element method (DEM) and CFD coupling method, the CFD-DEM coupled calcination research has been fully developed in recent years, and Bluhm-Drenhaus T et al. firstly realized the CFD-DEM coupled calculation of the calcination process in a PFR lime kiln, and carried out the simulation study on the gas and particle temperatures [26,27,28]. However, it is limited by the huge number of particles in the actual production, which has a large negative impact on the calculation efficiency. Meanwhile, the particle size in the PFR lime kiln is relatively homogeneous, which makes it unnecessary to use the DEM method, so the study of the calcination process based on the porous medium model is more relevant.

Duan et al [29] numerically modeled the calcination process in a PFR lime kiln under two mixed particle sizes, but the model was coarse and did not respond to the gas-solid situation in the whole domain. The mixed calcination of two particle sizes (also called sandwich calcination) is a common production form in PFR lime kilns, which not only improves the calcination efficiency, but also makes full use of the hard-to-utilize small pieces of raw materials, so this aspect of the research is of practical significance.

In summary, current research for PFR lime kilns has focussed on the ideal of uniform particle size decomposition, and researchers have lacked understanding of the mixed particle size proportioning process common in production. In this paper, the monitoring data of the recently commissioned PFR lime kiln is used to compare the simulation results, the mathematical model of limestone decomposition is improved, and numerical simulation is carried out according to the working conditions close to the actual production, and more convincing results are obtained, which are of practical significance for the optimisation of the process.

2. Mathematical models

The mass conservation equation is one of the basic equations in fluid dynamics, which is based on the continuous medium model as the theoretical basis and assumes that the variables such as time, density, temperature, etc. are continuously distributed in space, and its mathematical expression is shown in Equation 1.

$$\frac{\partial \rho}{\partial t} + \nabla \cdot (\rho \vec{v}) = S_m \tag{1}$$

Navier-Stokes equations are used to model gas flow and wind resistance variations, and the basic form of the equations is:

$$\frac{\partial (\rho \vec{v})}{\partial t} + \nabla \cdot (\rho \vec{v}\vec{v}) = -\nabla p + \nabla \cdot (\bar{\bar{\tau}}) + \rho \vec{g} + \vec{F} \tag{2}$$

The gas energy equation:

$$\frac{\partial}{\partial t}\left(\gamma \rho_{\mathrm{g}} c_{pg} T_{\mathrm{g}}\right) + \nabla\left(\gamma \vec{\mathrm{v}} \rho_{\mathrm{g}} c_{pg} T_{\mathrm{g}}\right) = \nabla \cdot \left(k_{\mathrm{g}} \nabla T_{\mathrm{g}}\right) - a_{\mathrm{v}} h_{\mathrm{v}}\left(T_g - T_0\right) \tag{3}$$

The solid energy equation:

$$\frac{\partial}{\partial t}((1-\gamma)\rho_{\mathrm{o}} c_{po} T_{\mathrm{o}}) + \nabla \cdot (\vec{\mathrm{v}}_{\mathrm{down}} (1-\gamma)\rho_{\mathrm{o}} c_{po} T_{\mathrm{o}}) = \nabla \cdot \left(\left(k_0 + e_{\mathrm{b}}\right)\nabla T_{\mathrm{o}}\right) + a_{\mathrm{v}} h_{\mathrm{v}}\left(T_{\mathrm{g}} - T_{\mathrm{o}}\right) \tag{4}$$

In this paper, a realizable k–ε turbulence model with Reynolds time-averaged method (RANS) is used in the simulation of turbulence calculation:

$$\frac{\partial}{\partial t}(\rho k) + \frac{\partial}{\partial x_i}(\rho k u_j) = \frac{\partial}{\partial x_i}\left[\left(\mu + \frac{\mu_t}{\sigma_{\mathrm{k}}}\right)\frac{\partial k}{\partial x_j}\right] + G_{\mathrm{k}} + G_{\mathrm{b}} - \rho\varepsilon - Y_{\mathrm{M}} + S_{\mathrm{k}} \tag{5}$$

$$\frac{\partial}{\partial t}(\rho \varepsilon) + \frac{\partial}{\partial x_i}(\rho \varepsilon u_j) = \frac{\partial}{\partial x_j}\left[\left(\mu + \frac{\mu_t}{\sigma_{\mathrm{k}}}\right)\frac{\partial \varepsilon}{\partial x_j}\right] + \rho C_1 S_{\varepsilon} - \rho C_2 \frac{\varepsilon^2}{k + \sqrt{\nu\varepsilon}} + C_{1\varepsilon}\frac{\varepsilon}{k} C_{3\varepsilon} G_b + S_{\varepsilon} \tag{6}$$

$$C_1 = \max\left[0.43\frac{\eta}{\eta+5}\right], \eta = S\frac{k}{\varepsilon}, \mu_{\mathrm{t}} = \rho C_{\mu}\frac{k^2}{\varepsilon}. \tag{7}$$

The advantage of the realizable k–ε model is that the calculation is more accurate for flat plate or cylindrical winding flow, while flow separation and flow mixing can be predicted more accurately.

In the limestone calcination process, the cooling air and high temperature flue gas are mixed in the lower part of the suspension chamber, while the exhaust gas will flow in the gap of the particles, so the realizable k–ε turbulence model is chosen to calculate the heat exchange process between the mixed gas and the particles more accurately.

The limestone is fed into the PFR lime kiln from the top and fills the space rapidly, so the limestone layer can be considered as a packed bed. When analyzing the gas-solid heat and mass exchange process, a porous medium model is needed to calculate the pressure drop when the fluid flows through the filled bed. It is usually solved using the Ergun equation:

$$\frac{|\nabla p|}{L}=\frac{150\mu(1-\gamma)^2}{D_p^2\gamma^3}v_\infty+\frac{1.75\rho(1-\gamma)}{D_p\gamma^3}v_\infty^2 \tag{8}$$

$$\frac{1}{\alpha}=\frac{150(1-\gamma)^2}{D_p^2\gamma^3},\ C_2=\frac{3.5(1-\gamma)}{D_p\gamma^3} \tag{9}$$

From the Ergun equation, it is found that the larger the particle size, the larger the voids formed by the stacking will be, and the pressure drop when the fluid flows through will be lower; on the contrary, if there are multiple particle sizes, the smaller particle size will fill the voids of the larger particle size to a certain extent, resulting in a larger pressure drop.

A shrinking core model has been applied to the decomposition of limestone particles with the following main components:

$$\frac{\partial r_{CaCO_3}}{\partial t}=-k\cdot\frac{M_{CaCO_3}}{\rho_{CaCO_3}}\cdot R_D \tag{10}$$

$$R_D=k_D\left(p_{eq}-p_{co_2}\right)\ R_D=k_D\left(p_{eq}-p_{co_2}\right) \tag{11}$$

$$k_D=0.0001\left(1+4.26Y_T\right)\exp\left(-\frac{4810}{T_p}\right) \tag{12}$$

$$p_{eq}=101325\exp\left[17.74-0.00108T_i+0.332\log(T_i)-22020/T_i\right] \tag{13}$$

$$Y_{T.C}=\begin{cases}\dfrac{480}{T_P-958} & T_P>1150\,\mathrm{K}\\ 2.5 & T_P\le 1150\,\mathrm{K}\end{cases} \tag{14}$$

$$\lambda=\frac{4\pi\lambda_1\lambda_2}{\lambda_1\left(\dfrac{1}{r_{c1}}-\dfrac{1}{r_{c2.m}}\right)+\lambda_2\left(\dfrac{1}{r_{c1.m}}-\dfrac{1}{r_{c1}}\right)} \tag{15}$$

A porous medium consists of a mixture of two particle sizes, and the porosities constituted by dual sizes with different mass ratios are different. Therefore, it is necessary to calculate the void fraction, i.e. the porosity of the porous medium, with the help of the DEM method.The DEM considers the motion of each particle (cell), at each moment, after being subjected to a force:

$$m_i\frac{\mathrm{d}v_i}{\mathrm{d}t}=\sum_{j=1}^{k_i}\left(\boldsymbol{F}_{cn,ij}+\boldsymbol{F}_{dn,ij}+\boldsymbol{F}_{ct,ij}+\boldsymbol{F}_{dt,ij}\right)+m_i\boldsymbol{g} \tag{16}$$

$$I_i\frac{\mathrm{d}\boldsymbol{\omega}_i}{\mathrm{d}t}=\sum_{j=1}^{k_i}\left(\boldsymbol{T}_{ij}+\boldsymbol{M}_{ij}\right) \tag{17}$$

DEM models can be categorized into two types: hard-sphere models and soft-sphere models. Soft sphere model collision occurs within a period of time, producing plastic deformation, mainly used to simulate the collision process between particles. The soft sphere

model has a wide range of applications, such as particle simulation calculations for packed beds, moving beds and fluidized beds.

The equation for solving the specific surface area during gas-solid convection heat transfer in a preheating shaft kiln is as follows:

$$a_v = (1-\gamma) \times \frac{S_p}{V_p} \tag{12}$$

Heat radiated from flue gas to pellets using the P-1 model:

$$-\nabla q_r = aG - 4a\sigma T^4 \tag{13}$$

3. Geometric modeling and operating principles

The 800 t/d PFR lime kiln, shown in Figure 1, has two identical chambers with a cross channel. Lump limestone is fed into Chamber 1 and descends by gravity. Passing through a fuel nozzle, it's heated by gas combustion, decomposing limestone to CO_2 and quicklime from surface to core. Cooling air is blown from Chamber 1's bottom to maintain quicklime's activity. Hot tail gas from calcination mixes with cooling air, enters Chamber 2 through the cross channel, preheating uncalcined limestone. Tail gas is discharged above Chamber 2. Chambers alternate every 15 minutes, boosting production, equipment durability, and waste heat utilization.

Each chamber of the PFR lime kiln has preheating, calcination, and cooling zones. Preheating zone (6 m tall) extends from the feeding port to the fuel nozzle bottom, with hot tail gas preheating stacked limestone. The calcination zone (9 m tall) begins below the fuel nozzle and continues as materials fall, making it the hottest area. The cooling zone (5 m tall) below the suspension cylinder rapidly cools the product. Mixed cooling air and hot flue gas form forced convection, enter Chamber 2, and the cooled quicklime exits Chamber 1.

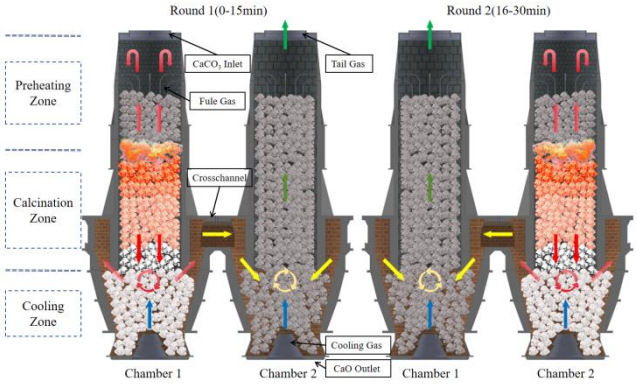

Figure 1. Fundamental Composition and Operating Principle of PFR Lime Kiln

Unlike rotary kilns, PFR kilns excel at calcining uniform particles, limiting capacity. Single-size calcination ensures uniform limestone decomposition, preventing unburnt large or over-burnt small particles from affecting product activity. PFR kilns support 40-120 mm particles, but crushing block limestone generates many < 30 mm particles. These dense materials affect air permeability and calcination. To avoid waste, PFR lime kilns use the

"sandwich calcination method," mixing large and small particles (5:1 ratio) for uniform calcination, optimizing flue gas diffusion and increasing kiln capacity.

The PFR lime kiln employs a low-calorie gas mixture, with the fuel lance's lower end serving as the temperature boundary. Calculations consider other boundary conditions, disregarding fuel gas premixing and combustion processes:

Table 1. Calculation conditions and values

Calculation condition	Value	Calculation condition	Value
Flue gas velocity/($m \cdot s^{-1}$)	5	Cooling gas inlet area/(m^2)	0.75×2
Flue gas inlets	64(chamber1)	$CaCO_3$ initial temperature/(K)	300
Flue gas initial temperature/(K)	1273	CaO density/($kg \cdot m^{-3}$)	3310
Tail gas outlet area/(m^2)	14.603	$CaCO_3$ density/($kg \cdot m^{-3}$)	2810
$CaCO_3$ inlet area/(m^2)	12.664	CaO thermal conductivity/($W \cdot m^{-1} \cdot K^{-1}$)	0.07
CaO outlet area/(m^2)	17.14	$CaCO_3$ thermal conductivity/($W \cdot m^{-1} \cdot K^{-1}$)	2.26
Cooling gas inlet velocity/($m \cdot s^{-1}$)	5	$CaCO_3$ decomposition temperature/(K)	1073

Due to the use of low calorific value gas in this equipment, the maximum particle size support 110 mm in single particle size calcination, so when using dual sizes calcination, the maximum particle size in the combination of particle size does not exceed 110 mm, the small particle size selection of 20 mm or 30 mm, the combination of the particle size of the void ratio as shown in Table 2.

Table 2. Void ratio in different particle sizes

Particle size combination/(mm)	Void ratio	Particle size combination/(mm)	Void ratio
110 + 30	0.2922	100	0.418
110 + 20	0.2657	90 + 30	0.3142
110	0.4187	90 + 20	0.2919
100 + 30	0.3084	90	0.4104
100 + 20	0.2723		

Comparing the void fraction of the three single sizes with the dual sizes, the void fraction of the layer mixed with 20 mm or 30 mm small sizes is reduced, which will have a significant impact on the calcination effect.

The PFR lime kiln's chambers alternate operation. After Chamber 1 starts, high-temperature gas fills the calcination zone in seconds, stabilizing while limestone particles decompose over 15 minutes. The gas-solid reaction time span is wide, justifying the unsteady-state method for Chamber 1 stability. Equations are solved with the semi-implicit method for velocity-pressure coupling, first-order upwind for turbulence equations, second-order upwind for others; convergence factor is 10^{-6}.

In the numerical calculations, it is assumed that the side walls of the furnace are adiabatic and do not exchange thermal mass with the outside. The particle size of quicklime after thermal decomposition of limestone remains constant. Both large and small particle sizes

are spherical, and heat exchange problems caused by complex surface features are not considered. In addition, the slight fragmentation problem caused by the downward movement of the particles will be ignored.

4. Results and Discussion

4.1. Modelling validation

The calculated values for the quasi-steady state do not vary with time and are therefore shown as a straight line in Fig. 2 and are convenient for comparison. In order to verify the reliability of the simulation results, the operating data of the 15 min production control platform were extracted and compared with the simulation results (Fig. 2a), and the results showed that the error between the real-time data of chamber temperature of the calcination zone temperature sensor (13 m height) and the simulation results of gas temperature were 3% and 4.5% (Fig. 2b), and the error between the real-time data of chamber temperature of the emission monitoring sensor (at the tail gas outlet) and the simulation results of gas temperature were 1.8% and 2.8% (Fig. 2c), indicating that the numerical simulation results of gas temperature and tail gas temperature are more reliable, which can reflect the distribution of gas temperature in the kiln.

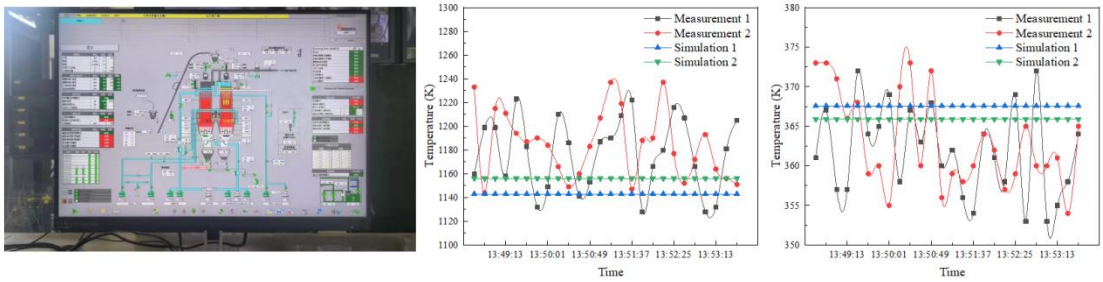

(a) (b) (c)

Figure 2 Comparison of simulation and production control system results
(a)-Control Platform; (b)-Gas temperature Validation; (c)-Tail gas temperature Validation

4.2. Gas temperature field

High-temperature gas enters calcination zone, affected by particle diameter, zone temperature reaches 800 K. Post-calcination gas enters preheating zone, with low temperature at its base (Fig. 3a). Mixed with 20 mm calcination zone particles, void ratio plummets, impeding gas flow & heat accumulation in material layer, creating > 1300 K zone covering calcination zone (Fig. 3b). Preheating zone gas temperature soars to 1000 K due to concentration. Gas agglomeration traps high-temperature flue gas in cooling zone, elevating its temperature. Mixing 30mm limestone reduces calcination zone gas agglomeration, narrowing > 1300 K zone, slightly cooling preheating zone, & allowing cooling air and high-temperature tail gas to converge in cooling zone, warming Chamber 2 (Fig. 3c).

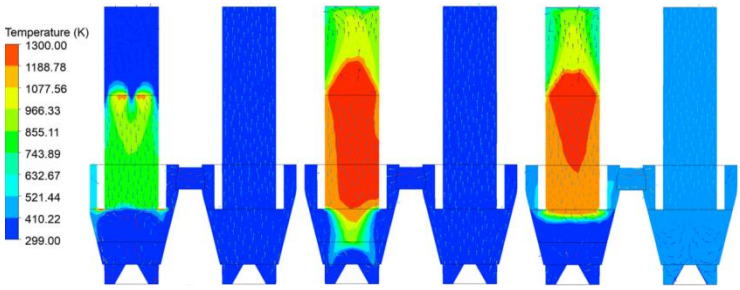

(a) (b) (c)

Figure 3. Gas temperature distribution at various particle sizes

(a)-90mm Single particle size; (b)-90+20mm dual sizes; (c)-90+30mm dual sizes

In Chamber 1 (Fig. 4a), temperature changes along gravity are similar, with small differences despite varying void ratios in 90 mm, 100 mm, and 110 mm layers. Max gas temperature in calcination zone is 900 K, with overall temperature range of 800~900 K. High-temperature tail gas after calcination mainly affects preheating zone at 10m~13m, resulting in weak preheating. In cooling zone, mixed gas with cooling air rapidly cools to room temperature. Mixing 20 or 30mm particles sharply decreases void ratio, enhancing high-temperature gas agglomeration. Calcined zone maintains high temperature (1200 K) similar to initial gas temperature, elevating preheating zone temperature. In cooling zone, 20 mm limestone-mixed gas cools slower, while 30 mm limestone-mixed gas cools faster. Chamber 1's gas temperature elevation correspondingly increases Chamber 2's temperature for preheating and energy saving. Mixed flue gas entering Chamber 2 from cross channel decreases linearly towards outlet. Faster temperature decrease with 20 mm particles indicates better waste heat utilization by dense layer. Tail gas discharge temperature is highest among the three single-size cases (Fig. 4b).

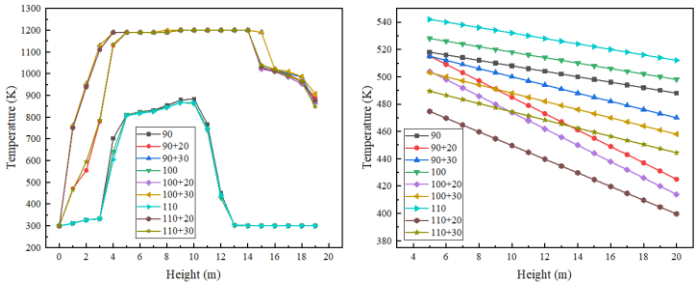

(a) (b)

Figure 4. Trend of gas temperature at various particle sizes

(a)-Chamber 1; (b)-Chamber 2

4.3. Solid temperature field

Limited by gas temperature, 90mm single-sized solids calcined near 700 K, below initial calcination temperature (Fig. 5a). Mixing small particles raised solids temperature, enhancing preheating with lower void ratio. However, 20 mm mixed layers cooled slowly in cooling zone, cooling gas struggled to penetrate dense layer, keeping solids hot longer, potentially reducing quicklime activity (Fig. 5b). Switching to 30 mm mix raised void ratio, improving cooling zone solids cooling. Mixed flue gases flowed easier through material layer, reaching Chamber 2 via cross channel, significantly boosting Chamber 2 solids temperature (Fig. 5c).

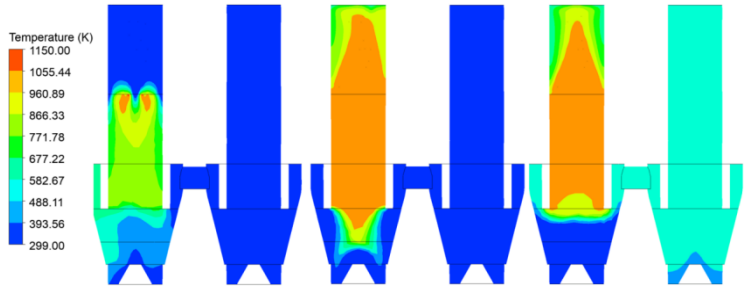

(a) (b) (c)

Figure 5. Solid temperature distribution at various particle sizes

(a)-90mm Single particle size; (b)-90+20mm dual sizes; (c)-90+30mm dual sizes

Solid temperature variations in Chamber 1 for all particle sizes resembled gas variations, with similar temperatures for all sizes. Smaller void fraction differences among three sizes resulted in reduced lime kiln layer temperature gradient (Fig. 6a). Mixing 20 mm particles decreased void ratio, making it harder for high-temperature gas to pass, stabilizing layer temperature below 1100 K. Solid temperatures were notably lower than with 30 mm mix. Chamber 1's solid temperature changes suggest optimal heating efficiency with moderate void ratios. High-temperature flue gas mixed with cooling air preheat solids in Chamber 2. Unlike Chamber 2, solid temperature changes with height showed rapid (dual sizes) and slow (single size) decreases. Single-size gas entered Chamber 2 cooler, providing uniform but less intense heating. Dual sizes provided better preheating but denser bed, faster gas temperature drop, poorer preheating, and lower solid temperatures in Chamber 2's upper region (Fig. 6b).

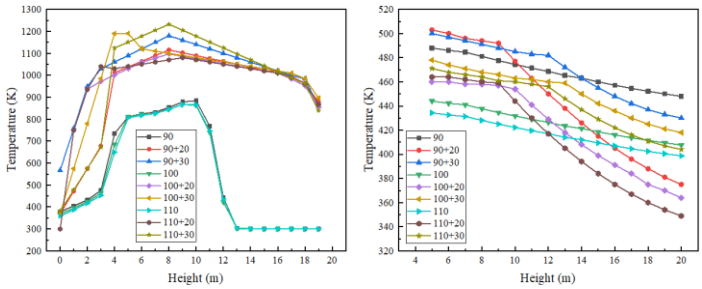

(a) (b)

Figure 6. Trend of solid temperature at various particle sizes

(a)-Chamber 1; (b)-Chamber 2

4.4. Calcination Effect Distribution

Low-grade fuel gas failed to fully decompose 90 mm limestone particles, with only 10 mm thickness decomposing near gas inlet (Figure 7a). Mixing 20 mm limestone greatly improved decomposition efficiency, especially for 90 mm particles, resulting in complete decomposition in calcining and cooling zones (Figure 7b). With 30 mm limestone, void ratio increased, calcination effect fell between single and 20 mm mixed sizes. Solids reacted more fully in calcining zone, but some cooled incompletely in cooling zone, increasing undecomposed thickness (Figure 7c).

Based on undecomposed thickness, single-sized particle decomposition conditions were inadequate. 90 mm, 100 mm, and 110 mm reacted differently when mixed, with complete decomposition heights varying between 90 mm mixed with 20 mm and 30 mm (Fig. 8a), but all completed below 12 m. 100 mm particles mixed with 30 mm limestone had slightly higher

decomposition than with 20 mm. For 100 mm mixed with 30 mm, undecomposed particle thickness in calcination zone was higher than for 20+30 mm mixed, indicating insufficient thermal energy for large and small particles' decomposition (Fig. 8b). In 110mm mixed grain calcination, both 20 mm and 30 mm grains had minimal effect on large grain decomposition, with calcination effect no worse than for 100 mm mixed (Fig. 8c). In contrast, single-sized particle decomposition showed dual sizes significantly improved layer densification and calcination.

The ratio of decomposed thickness to solid particle radius assessed calcination effect of large (90, 100, 110mm) and small (20, 30mm) particle mixes (Fig. 9). 100 + 20 mm mix had lowest decomposition rate, followed by 90 + 20 mm and 110 + 20 mm, with 30 mm mixes nearly equal. Undecomposed ratios were similar for 30 mm mixes. Void rate distribution alone isn't a perfect calcination indicator; optimal material layer density isn't always denser, as too low a void rate hinders gas flow, affecting calcination.

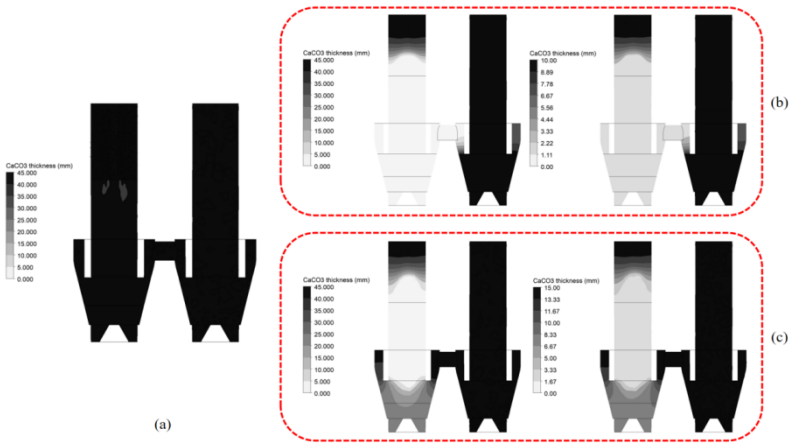

Figure 7. Undecomposed thickness distribution

(a)-90mm Single particle size; (b)-90+20mm dual sizes; (c)-90+30mm dual sizes

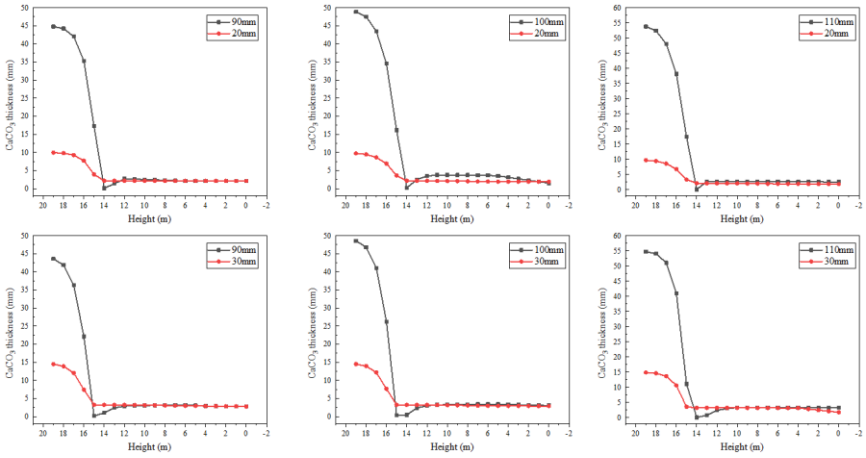

(a) (b) (c)

Figure 8. Decomposition trends at dual sizes

(a)-90mm; (b)-100mm; (c)-110mm

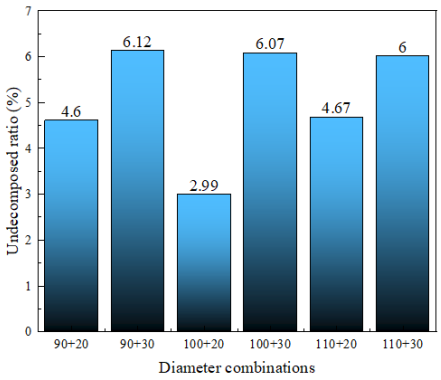

Figure 9. Comparison of undecomposed ratio of dual particle sizes

5. Conclusions

PFR lime kiln is widely used in iron and steel metallurgy field for supporting various types of fuel and high active quality. A large amount of low-grade fuel gas generated in various processes of iron and steel smelting needs to be utilized urgently, and the exploration of related technologies has become an important research direction for the new low-carbon method of calcining limestone. This paper establishes a mathematical model for the calcination process of dual sizes limestone under the condition of fixed mass fractions based on the theory of PMM. The accuracy of the model is verified by comparing the numerical simulation results with the production data.

It was shown that the undecomposed problem caused by the use of low-grade fuel for large-grained limestone calcination was improved by mixing 20mm or 30mm small-grained limestone particles to reduce the layer void ratio and increase the concentration effect of high-temperature gas in the layer. The decomposition rate of limestone is basically the same after mixing 30mm particle size with 90 mm, 100 mm and 110 mm respectively, and the improvement of decomposition rate is limited when 20 mm limestone is further mixed into 90 mm, 100 mm and 110 mm as a small particle size, while the agglomeration effect leads to slower cooling of quicklime which may cause overcooking problem. Therefore, numerical simulation using dual particle size can effectively fit the particle size combination for calcination.

In addition, based on the large difference in diffusion time scales between gas and solid, this study used a quasi-steady-state method instead of a unsteady state method for calculating limestone calcination, which achieves fast convergence and not only saves the calculation time, but also ensures the accuracy of the calculation.

Nomenclature

C_2	- Inertial resistance coefficient	R_D	- Limestone decomposition rate
C	- Linear anisotropic phase function coefficients	S_G	- Radiation source term, [W/m^2]
C_{pg}	- Specific heat capacity of gas,	S_m	- Fluid mass from discrete to

	[kJ/kg/K]		continuous phase, [kg/m^3/s]
C_{p0}	- Specific heat capacity of solids, [kJ/kg/K]	t	- Time, [s]
D_p	- Diameter of particles, [mm]	T_0	- Solid temperature, [K]
d_{caco3}	- Diameter of the internal core calcium carbonate, [mm]	T_g	- Gas temperature, [K]
$\vec{F}$	- External force, [kg/m/s^2]	T_i	- Temperature of internal core, [K]
$\boldsymbol{F}_{cn,ij}$	- Directional contact force, [N]	T_p	- Average particle temperature, [K]
$\boldsymbol{F}_{ct,ij}$	- Tangential contact force, [N]	$\boldsymbol{T}_{ij}$	- Tangential moment, [N·m]
$\boldsymbol{F}_{dn,ij}$	- Directional damping force, [N]	v	- Fluid velocity, [m/s]
$\boldsymbol{F}_{dt,ij}$	- Tangential damping force, [N]	$\boldsymbol{v}_i$	- The advection velocity of particle i, [m/s]
G_b	- Buoyancy turbulent kinetic energy, [J]	Y_M	- Pulsating expansion impact factor
G_k	- Velocity turbulent kinetic energy, [J]	$Y_{T.C}$	- Reaction rate correction factor
h_V	- Gas-solid convection heat transfer coefficient, [W/m^2/K]		***Greek symbols***
I_i	- Moment of inertia, [kg·m^2]	α_v	- Specific surface area of solid, [m^2]
l_Z	- Feature length, [m]	$1/\alpha$	- Coefficient of viscous resistance
k_D	- Reaction constants	β	- Radiation convergence coefficient
k_i	- Number of particles in contact with particle i	ρ	- Continuous medium density, [kg/m^3]
m_i	- Mass of particle i, [kg]	λ_1	- Thermal conductivity of internal core, [W/m/K]
M_{CaCO_3}	- Relative molecular mass of calcium carbonate, [mm]	λ_2	- Thermal conductivity of external core, [W/m/K]
$\boldsymbol{M}_{ij}$	- Rolling friction torque, [N·m]	ρ_{CaCO_3}	- Density of the calcium carbonate, [kg/m^3]
p	- Static pressure, [Pa]	ρ_g	- Gas density, [kg/m^3]
p_{co_2}	- CO_2 partial pressure in the environment, [Pa]	ρ_0	- solid density, [kg/m^3]

p_{eq}	- Equilibrium partial pressure, [Pa]	σ_k	- κ equation Prandtl number
r_{c1}	- Calcium carbonate radius, [mm]	σ_ε	- ε equation Prandtl number
$r_{c1.m}$	- 1/2 calcium carbonate radius, [mm]	$\overline{\overline{\tau}}$	- stress tensor, [Pa]
$r_{c2.m}$	- Calcium carbonate radius plus 1/2 CaO layer radius, [mm]		

References

[1] Deng, T., *et al.*, Limestone Dissolution in Converter Slag at 1873 K (1600 °C), *Metall Mater Trans B*, 44 (2013), pp. 98-105

[2] Hamano, T., *et al.*, Reaction Mechanism between Solid CaO and FeO_x–CaO–SiO_2–P_2O_5 Slag at 1573 K, *ISIJ International*, 46(2006), 4, pp. 490-495

[3] Thumsorn, S., *et al.*, Thermal decomposition kinetic and flame retardancy of $CaCO_3$ filled recycled polyethylene terephthalate/recycled polypropylene blend, *Journal of Applied Polymer Science*, 127(2012), 2, pp. 1245-1256

[4] L'vov., *et al.*, Kinetic parameters of $CaCO_3$ decomposition in vacuum, air and CO2 calculated theoretically by means of the thermochemical approach, *Reac Kinet Mech, Cat*, 114(2015), pp. 31-40

[5] Chen, M., *et al.*, Limestone Dissolution in Converter Slag: Kinetics and Influence of Decomposition Reaction, *ISIJ International*, 8(2018), 12, pp. 2271-2279

[6] Galai, H., *et al.*, Mechanism of growth of MgO and $CaCO_3$ during a dolomite partial decomposition, *Solid State Ionics*, 178(2007), A15-18, pp. 1039-1047

[7] Mastorakos, E., *et al.*, CFD predictions for cement kilns including flame modeling, heat transfer and clinker chemistry, *Applied Mathematical Modelling*, 23(1999), 1, pp. 55-76

[8] Yuan, J., *et al.*, Using process modelling to improve lime kiln operations, *Pulp and paper Canada*, 104(2003), 11, pp. 41-44

[9] Meier, A., *et al.*, Multitube Rotary Kiln for the Industrial Solar Production of Lime, *Journal of Solar Energy Engineering*, 127(2005), 3, pp. 386-395

[10] Liu, Z., *et al.*, Optimizing pre-reduction of vanadium–titanium magnetite through recycling and integrating of top gas from melting furnace and tail gas from rotary kiln, *Process Safety and Environmental Protection*, 185(2024), pp. 86-95

[11] Sarrafi, A., *et al.*, CFD simulation of gas flow in a rotary kiln: Validation and similarity for an industrial scale kiln, *Chemical Technology*, 9(2014), 1, pp. 22-26

[12] Metzger, M., *et al.*, Maerz kiln redesign partnership improves lime production by 30%, *Cement International*, 12(2014), 3, pp. 54-57

[13] José, U.J., *et al.*, Dynamic modeling of the heat transfer process in rotary kilns with indirect oil heating: Parametric analysis of gypsum calcination case, *Thermal Science*, 26(2022), 2, pp. 1637-1648

[14] Benanti, E., *et al.*, Simulation of olive pits pyrolysis in a rotary kiln plant, *Thermal Science*, 15(2011), 1, pp. 145-158

[15] Vola, G., *et al.*, Investigation and prediction of marble mechanical degradation and dust formation during calcination process in Twin Shaft Regenerative (TSR) kilns, *Cement*

International, 13(2005), 3, pp. 42-47
[16] Haido, D., *et al.*, Simulation of lime calcination in PFR kiln - Influence of energy input and lime throughput, *Zkg International*, 64(2011), 12, pp. 52-63
[17] Haido, D., *et al.*, Simulation of lime calcination in PFR kilns - Influence of source and size of limestone, *Zkg International*, 65(2012), 4, pp. 56-65
[18] Filkoski, R.V., *et al.*, Energy optimisation of vertical shaft kiln operation in the process of dolomite calcination, *Thermal Science*, 22(2018), 5, pp. 2123-2135
[19] Cristea, E.D., *et al.*, Utilization of lean gases in lime burning with regenerative kilns, *Zkg International*, 56(2003), 6, pp. 58-64
[20] Ommerborn, T., *et al.*, Simplifying the geometry of a parallel-flow regenerative (PFR) kiln to achieve both long-term cost savings and process advantages, *Zkg International*, 71(2018), 12, pp. 64-67
[21] Mohammadpour, K., *et al.*, CFD simulation of reactive flow in parallel flow regenerative shaft kilns using porous media model, *Thermal Science*, 26(2022), 2, pp. 1175-2183
[22] Mohammadpour, A.S.E., *et al.*, CFD simulation of cross-flow mixing in a packed bed using porous media model and experimental validation, *Computational particle mechanics*, 6(2018), 3, pp. 157-162
[23] Roberto, A., *et al.*, CFD Analysis of Co-firing of Coke and Biomass in a Parallel Flow Regenerative Lime Kiln, *Waste and biomass valorization*, 13(2022), 12, pp. 4925-4949
[24] Piringer, H., *et al.*, New PFR Lime Kiln Process with Blast Furnace Gas and Oxygen, *ZKG Cement Lime Gypsum*, 74(2021), 8, pp. 42-25
[25] Duan, S., *et al.*, Numerical Simulation Study of Gas-Solid Heat Transfer and Decomposition Processes of Limestone Calcined with Blast Furnace Gas in a Parallel Flow Regenerative Lime Kiln, *Materials*, 15(2022), 11, 4024
[26] Bluhm, D.T., *et al.*, A coupled fluid dynamic-discrete element simulation of heat and mass transfer in a lime shaft kiln, *Chemical Engineering Science*, 65(2010), 9, pp. 2821-2834
[27] Deen, N.G., *et al.*, Direct numerical simulation of fluid flow accompanied by coupled mass and heat transfer in dense fluid–particle systems, *Chemical Engineering Science*, 116(2014), 36, pp. 645-656
[28] Jian, Q., *et al.*, Numerical study of particle behaviours and heat transfer in a complex rotary kiln, *Particuology*, 92(2024), pp. 81-94
[29] Duan, S., *et al.*, Numerical Simulation Study of Mixed Particle Size Calcination Processes in the Calcination Zone of a Parallel Flow Regenerative Lime Kiln, *Materials*, 15(2022), 13, 4609

Submitted: 12.04.2024.
Revised: 03.06.2024.
Accepted: 08.06.2024.